

See discussions, stats, and author profiles for this publication at: <https://www.researchgate.net/publication/272421908>

# Homogeneous Nucleation of Predominantly Cubic Ice Confined in Nanoporous Alumina

ARTICLE in NANO LETTERS · MARCH 2015

Impact Factor: 13.59 · DOI: 10.1021/nl504855z · Source: PubMed

CITATION

1

READS

96

6 AUTHORS, INCLUDING:



**Hatice Duran**

TOBB University of Economics and Technology

40 PUBLICATIONS 512 CITATIONS

SEE PROFILE



**Martin Steinhart**

Universität Osnabrück

181 PUBLICATIONS 5,421 CITATIONS

SEE PROFILE



**Michael Kappl**

Max Planck Institute for Polymer Research

143 PUBLICATIONS 3,894 CITATIONS

SEE PROFILE



**George Floudas**

University of Ioannina

229 PUBLICATIONS 4,182 CITATIONS

SEE PROFILE

# Homogeneous Nucleation of Predominantly Cubic Ice Confined in Nanoporous Alumina

Yasuhito Suzuki,<sup>†</sup> Hatice Duran,<sup>‡</sup> Martin Steinhart,<sup>§</sup> Michael Kappl,<sup>†</sup> Hans-Jürgen Butt,<sup>†</sup> and George Floudas<sup>\*,||</sup>

<sup>†</sup>Max-Planck Institute for Polymer Research, 55128 Mainz, Germany

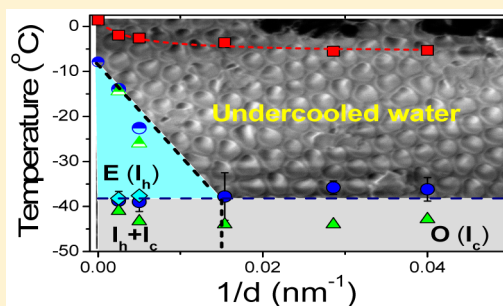
<sup>‡</sup>Department of Materials Science and Nanotechnology Engineering, TOBB University of Economics and Technology, 06560 Ankara, Turkey

<sup>§</sup>Institut für Chemie neuer Materialien, Universität Osnabrück, D-49069 Osnabrück, Germany

<sup>||</sup>Department of Physics, University of Ioannina, 45110 Ioannina, Greece

## **S** Supporting Information

**ABSTRACT:** The nucleation mechanism of water can be precisely regulated by confinement within nanoporous alumina. We found a transition from heterogeneous nucleation of hexagonal ice ( $I_h$ ) to homogeneous nucleation of predominantly cubic ice ( $I_c$ ) with decreasing pore diameter. These results lead to a phase diagram of water under confinement. It contains a (stable) predominant  $I_c$  form, a form known to exist only in the upper atmosphere. Possible applications range from cryopreservation to construction materials like cement.



**KEYWORDS:** Ice nucleation, cubic ice, confined crystallization, homogeneous nucleation

Liquid water can be supercooled down to  $-38\text{ }^{\circ}\text{C}$ , known as the limit of homogeneous nucleation.<sup>1,2</sup> In most cases, however, water will freeze at higher temperatures by impurities via heterogeneous nucleation. This is also the main crystallization process in cloud droplets triggered by dust or biological aerosols.<sup>3,4</sup> However, despite fundamental importance in science and technology control of heterogeneous and, more importantly, of homogeneous nucleation at atmospheric conditions remains a challenge. Here we show that the nucleation mechanism can be precisely regulated by confining water within self-ordered nanoporous aluminum oxide (AAO)<sup>5</sup> with pore diameters ranging from 400 nm down to 25 nm. Confined water exists in globular proteins, cloud nuclei, and icy interstellar particles with respective implications to molecular biology, atmospheric chemistry and interstellar physics and chemistry. Furthermore, controlling ice formation is essential for the durability of building materials like cement.

When freezing bulk water from ambient temperature it solidifies to hexagonal ice ( $I_h$ ).<sup>6</sup> Indications for naturally formed cubic ice ( $I_c$ ) have only been found in the upper atmosphere. Whalley,<sup>7</sup> for example, suggested that the well-known Scheiner's halo around the sun or the moon is caused by light passing at an angle of minimum deviation through octahedral crystals of  $I_c$ . Later a partial  $I_c$  phase was reported by rapid quenching of water droplets,<sup>8</sup> by condensation of vapor in a supersonic flow<sup>9</sup> and during the homogeneous freezing of aqueous droplets suspended in an oil matrix.<sup>10</sup> Partial  $I_c$  has also been reported by annealing the amorphous phase,<sup>11</sup> by

recrystallization from high-pressure phases<sup>12,13</sup> and by freezing of water in nanoporous silica.<sup>14–19</sup> More recently, it has been suggested that the metastable  $I_c$  is a stacking-disordered material containing cubic sequences interlaced with hexagonal sequences, a structure termed stacking-disordered ice (i.e., ice  $I_{sd}$ ).<sup>20,6</sup> In addition, a hidden metastable phase, named Ice 0, was suggested to control homogeneous nucleation.<sup>21</sup> Apart from the crystal form of ice, little is known on the mechanism of ice nucleation (heterogeneous vs homogeneous) under confinement. Herein, we employ AAO, which contains arrays of discrete, parallel, and cylindrical nanopores with uniform pore length and diameter,<sup>5</sup> as a model system to study the effect of confinement on water crystallization. The defined geometry of pores in AAOs (where the pores themselves are not porous) also stimulated recent studies of liquid crystal<sup>22,23</sup> as well as of polymer crystallization under confinement.<sup>24–27</sup>

Self-ordered AAO with a pore depth of 100  $\mu\text{m}$  and the specified pore diameter was prepared according to procedures reported elsewhere.<sup>5</sup> Low-temperature scanning electron microscopy (SEM) images were acquired with a Nova600 NanoLab – Dualbeam SEM/focused ion beam (FIB) system equipped with a cryogenic preparation chamber (Quorum Technologies) using a “through the lens” secondary electron

**Received:** December 18, 2014

**Revised:** February 10, 2015



detector. Water containing 20 wt % CsCl (necessary to make water “visible” only in the SEM/FIB study) was infiltrated into the AAO membranes (Supporting Information, Section A.2). The  $\Theta/2\Theta$  scans were made with a D8 Advance X-ray diffractometer (Bruker) from AAO/water samples milled to powder and inserted to 2 mm glass capillaries (Supporting Information Figure S2) as well as from unmodified AAO/water templates) (Figures 1c and 2). Scans in the  $2\Theta$ -range from 1 to

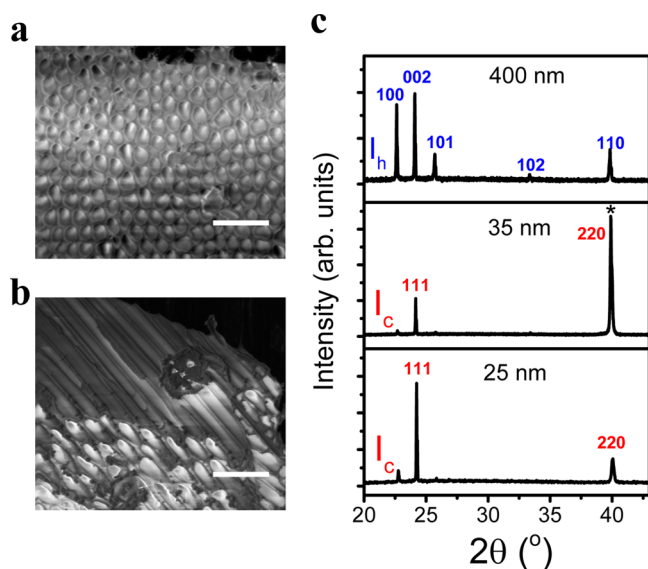


**Figure 1.** SEM images of confined ice (left) and diffraction patterns of water frozen inside AAO (right). (a) SEM top view (top) and (b), side view of water frozen at  $-100\text{ }^{\circ}\text{C}$ . The white bar corresponds to  $2\text{ }\mu\text{m}$  length. (c) Water frozen at  $-50\text{ }^{\circ}\text{C}$  within AAO with different pore diameters: 400 nm (top), 35 nm (middle), and 25 nm (bottom). In this configuration the AAO pore axes are oriented parallel and the AAO surface oriented perpendicularly to the plane of the incident and scattered X-ray beams. The main reflections corresponding to hexagonal ice ( $I_h$ ) and to cubic ice ( $I_c$ ) are shown in blue and red, respectively. The star indicates background scattering (Al).

$45\text{ }^{\circ}\text{C}$  in steps of  $0.01^{\circ}$  were made at  $-50\text{ }^{\circ}\text{C}$  after fast cooling ( $50\text{ }^{\circ}\text{C}/\text{min}$ ) from ambient temperature (Supporting Information, Section A.3). Additional measurements were made subsequently at  $-10\text{ }^{\circ}\text{C}$  to address the stability of the formed phase. Thermal analysis was carried out using a Mettler Toledo differential scanning calorimeter (DSC-822). Prior to DSC measurements, the Al substrates to which the AAO membranes had been connected, were etched away by using a mixture of HCl,  $\text{CuCl}_2$ , and  $\text{H}_2\text{O}$ . The AAO membranes were weighed with a Mettler Toledo AX205 balance, infiltrated with water, and finally milled to powder. Subsequently, 1.2–3.7 mg of sample material was sealed in aluminum pans ( $100\text{ }\mu\text{L}$ ). DSC traces of water-infiltrated AAO were recorded using reference pans containing empty AAO pieces of the same pore diameter. All samples were first cooled at a rate of  $50\text{ }^{\circ}\text{C}/\text{min}$  from ambient temperature to  $-100\text{ }^{\circ}\text{C}$  and then heated to  $30\text{ }^{\circ}\text{C}$  at the same rate under a nitrogen atmosphere (Supporting Information, Section A.4). Dielectric measurements were performed as a function of temperature in the range from  $-90$  to  $20\text{ }^{\circ}\text{C}$  at atmospheric pressure under isochronal conditions ( $f = 1\text{ MHz}$ ) using a Novocontrol Alpha frequency analyzer (frequency range from  $10^{-2}$  to  $10^6\text{ Hz}$ ). For bulk water, the DS measurements were carried out with a Novocontrol cylindrical cell with electrodes of 10 mm in

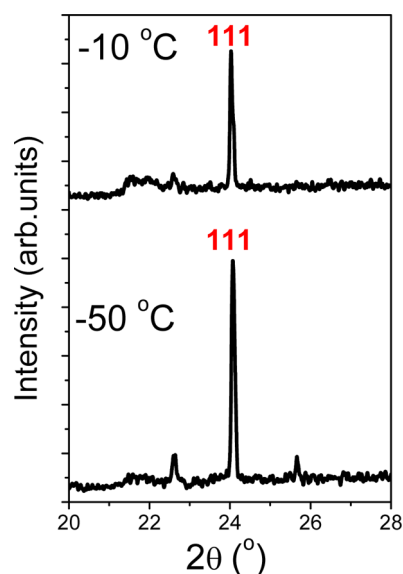


**Figure 2.** Diffraction patterns of water frozen inside AAO with pore diameter of 35 nm (bottom) at  $-50\text{ }^{\circ}\text{C}$  and following subsequent heating to  $-10\text{ }^{\circ}\text{C}$  (top). The main reflection (111) from cubic ice is indicated.

diameter and a sample thickness of 1 cm. For water-infiltrated self-ordered AAO samples, a 10 mm electrode was placed on top of the templates whereas the Al in the bottom of the templates served as the second electrode (Supporting Information, Section A.5).

Figure 1 a,b shows SEM images of water frozen at  $-100\text{ }^{\circ}\text{C}$  revealing fully filled pores. Diffraction patterns of ice within AAO with a pore diameter of 400 nm at  $-50\text{ }^{\circ}\text{C}$  show relative peak intensities significantly differing from those of bulk water:<sup>6</sup> the (111) and (220) reflections were more intense, but the structure is still identified as  $I_h$  (Figure 1c). When reducing the pore diameter to 35 and 25 nm, the diffraction patterns were fundamentally different. The dominant peaks correspond to the (111) and (220) reflections of cubic ice ( $I_c$ ). A minor feature is some remaining peaks from the  $I_h$  structure most likely due to condensation at the AAO surface and/or due to the formation of ice  $I_{sd}$  containing a small amount of stacking faults.<sup>20</sup> To the best of our knowledge, under atmospheric conditions such diffraction patterns corresponding to a predominantly cubic ice at  $-50\text{ }^{\circ}\text{C}$  have not been reported previously. This form is stable under annealing and persists up to the melting point as shown in the diffraction patterns of Figure 2 obtained at  $-50\text{ }^{\circ}\text{C}$  and subsequently at  $-10\text{ }^{\circ}\text{C}$ . Both patterns indicate a predominantly  $I_c$  form. To further emphasize this point, a comparison of previously reported X-ray diffraction patterns for unconfined and confined ice with the present case is made in Figure S1, Supporting Information.

The suppression of the hexagonal and the dominance of cubic phase in AAO pores having diameters  $\leq 35\text{ nm}$  can be understood if we compare the size of the critical nuclei,  $l^*$ , with respect to the pore size,  $d$ . It is known that certain metastable crystalline phases can be stabilized within nanoporous materials such as AAOs.<sup>28</sup> This may reflect the relation of the critical nucleus size to the degree of undercooling,  $\Delta T$ . Phases formed at small undercooling have large nuclei that are most affected by confinement. In the smaller pores only phases having  $l^* < d$  are stable. On the basis of this finding, the radius of the critical

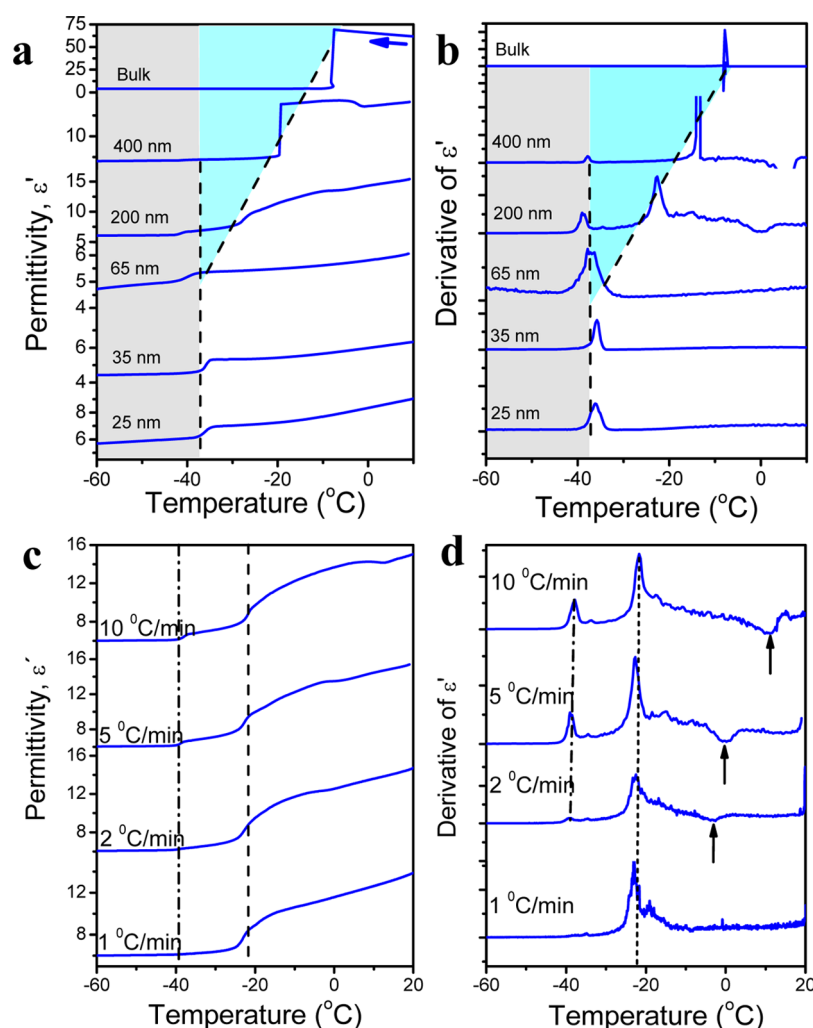


**Figure 3.** Temperature dependence of the dielectric permittivity for bulk water and water inside AAO measured at 1 MHz. (a) Permittivity obtained on cooling with  $5^{\circ}\text{C}/\text{min}$ . Gray and blue areas correspond to ice formation via homogeneous and heterogeneous nucleation, respectively. (b) Derivative of dielectric permittivity,  $d\epsilon'/dT$ , as a function of temperature. (c) Permittivity of water in AAO with a pore diameter of 200 nm measured at different cooling rates. Vertical dashed and dash-dotted lines indicate the characteristic temperatures of heterogeneous and homogeneous nucleation, respectively. (d) Derivative of dielectric permittivity curves of panel c as a function of temperature. Arrows indicate the rate dependence of the density anomaly of water in the 200 nm pores.

nucleus for the  $I_c$  phase is below  $\sim 17$  nm, which is in excellent agreement with a thermodynamic estimate from Johari.<sup>29</sup>

The high dielectric permittivity of water and its temperature-dependence can be employed as a fingerprint of the mechanism of ice nucleation. The notion that the temperature of freezing is coupled to the actual nucleation mechanism is not new but is based on several studies in crystallizable polymers within the same AAOs by the present group.<sup>24–27</sup> These studies have shown that homogeneous nucleation is the dominant mechanism at lower temperatures in the smaller pores. Figure 3a compares the dielectric permittivity of bulk water measured at a frequency of 1 MHz with water in AAO for pore diameters ranging from 400 down to 25 nm. At the cooling rate of  $5^{\circ}\text{C}/\text{min}$ , bulk water freezes at  $-7.9^{\circ}\text{C}$ . The bulk dielectric permittivity first increases on cooling and below freezing assumes a low value corresponding to the limiting high-frequency permittivity of hexagonal ice of  $\epsilon'_{\infty} \sim 3.2$ . The dielectric permittivity of water inside AAO with a pore diameter of 400 nm was substantially different (Supporting Information Figure S3). First, the permittivity had a tendency to decrease upon cooling except in the range from  $7.5$  to  $1.2^{\circ}\text{C}$  where it

increased by 7.5%. The overall decrease was due to the unavoidable fact that during the experiment a small amount of water evaporated. The steep increase likely reflects changes of the effective dipole moment due to dipole–dipole interactions (the Kirkwood factor). Upon further cooling, water froze at  $-13.6^{\circ}\text{C}$  to a permittivity of  $\sim 4$ . The derivative of the dielectric permittivity with respect to temperature (Figure 3 b) revealed another minor feature at  $\sim -38^{\circ}\text{C}$ , which is the reported lowest temperature for water crystallization via homogeneous nucleation.<sup>1</sup> The step in dielectric permittivity at this temperature is  $\Delta\epsilon \sim 0.16$ , that is, only a fraction of the step at  $-13.6^{\circ}\text{C}$  ( $\Delta\epsilon \sim 12.4$ ). On the basis of this, we conclude that the majority of pores contain impurities that initiate crystallization by heterogeneous nucleation. However, about 1% of pores are either free from such heterogeneities or the nucleation mechanism in these pores is very slow (see below). In AAO with a pore diameter of 200 nm, first a shallow increase in dielectric permittivity in the range from  $1.5$  to  $-1.7^{\circ}\text{C}$  was observed, followed by stepwise decreases at  $-22.7$  and  $-38.9^{\circ}\text{C}$  attributed to heterogeneous and homogeneous nucleation, respectively.

Crystallization in the smaller pores was fundamentally different. Only a single step in dielectric permittivity was observed in the range from  $-36$  to  $-38$  °C. For the 65 nm pores, we could instead distinguish two broad peaks in the derivative of the permittivity at  $-36$  and  $-38$  °C. These results can be interpreted by assuming that heterogeneous nucleation become less and less likely the smaller the pores become. The reduced propensity for heterogeneous nucleation in the smaller pores can be discussed by water heterogeneities that are excluded in the smaller pores. This suggests that the size of most common heterogeneities in water exceed 35 nm. Indeed, biological impurities such as bacteria as well as several viruses have sizes above 35 nm.<sup>4</sup> Alternatively, the pore curvature may also play some role in suppressing crystallization.<sup>30</sup> The value of the dielectric permittivity at low temperatures ( $-90$  °C) in AAO was higher than the limiting high-frequency permittivity of bulk ice ( $\epsilon'_{\infty} \sim 3.2$ ) suggesting the presence of some undercooled water. Using the values of  $\epsilon'_{\infty}$  of ice, we estimate that a fraction of 1.4 and 1.9% of water exists within the 400 and 65 nm pores, respectively (Supporting Information). As to the relation between undercooled water and the presence of interfacial water, more studies are needed to elucidate their dielectric properties.

The extent of homogeneous nucleation as compared to heterogeneous nucleation increased with increasing cooling rate, as shown in Figure 3 c,d for water crystallizing in AAO with pore diameter of 200 nm. At relatively high cooling rates, both heterogeneous and homogeneous nucleation was observed at  $-23$  and at  $-38$  °C, respectively. When cooling very slowly, that is, with merely 1 °C/min, heterogeneous nucleation dominated. This indicates that all 200 nm pores contain heterogeneities that can ignite crystallization. However, at the faster cooling rates, heterogeneous nucleation can be suppressed for kinetic reasons. In contrast, in AAO with pore diameters of 35 and 25 nm, water crystallization is exclusively initiated by homogeneous nucleation, independent of the cooling rate (Supporting Information Figures S4, and S5).

These results on ice formation under uniform confinement are further supported by differential scanning calorimetry (DSC). Figure 4 a shows DSC traces of water inside AAOs at a cooling rate of 10 °C/min. Under these conditions, water inside 400 nm pores freezes predominantly at  $-10$  °C via

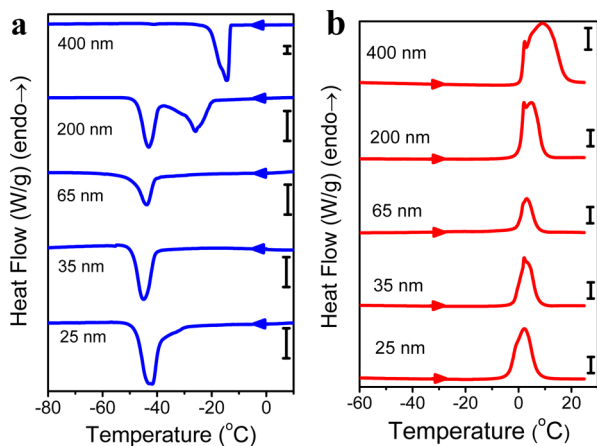


**Figure 4.** Differential scanning calorimetry traces of water inside AAO. (a) DSC traces obtained upon cooling with 10 °C/min. (b) DSC traces obtained upon heating with 10 °C/min immediately following (a). The vertical bar indicates a scale of 1 W/g.

heterogeneous nucleation with a smaller exothermic peak at  $-42$  °C revealing some homogeneous nucleation. In AAOs with 65 nm pores, two processes at  $-34$  and at  $-42$  °C were observed, reflecting ice formation via heterogeneous and homogeneous nucleation, respectively. For even smaller pores (35 and 25 nm), water freezes solely via homogeneous nucleation in agreement with dielectric spectroscopy results. Figure 4b depicts the corresponding melting curves. The higher than 0 °C melting temperature is due to the (high) heating rate. There is significant depression of the melting temperature with decreasing pore diameter. In addition, as has been observed earlier,<sup>31</sup> the enthalpy of melting is also decreasing with pore size. For example, for ice inside AAOs with 400 nm pores the enthalpy of melting is 3.5 kJ/mol whereas within 25 nm pores it is only 2.4 kJ/mol, that is, a fraction of the bulk value ( $\sim 5.9$  kJ/mol).<sup>32</sup> Although this reduction is beyond the expected one based on the lower crystallization temperatures within the 400 and 25 nm pores,<sup>32</sup> we cannot make more quantitative discussion for all pores because of some evaporation during sample preparation in DSC.

Ice formation in AAO can be summarized in a “phase diagram” (Figure 5). The proposed temperature versus

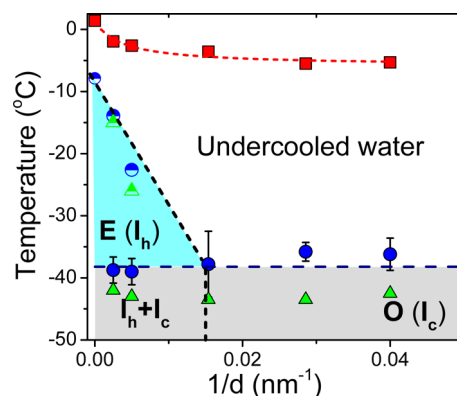


**Figure 5.** Effective phase diagram of water located inside self-ordered AAO. The squares indicate the melting temperatures as a function of inverse pore diameter. The red-dashed line is the result of a fit to the Gibbs–Thomson equation. The half-filled circles indicate heterogeneous nucleation whereas the completely filled circles homogeneous nucleation as obtained from dielectric spectroscopy. Half-filled and completely filled triangles give the respective transition temperatures obtained from DSC. Gray and blue areas correspond to ice formation via homogeneous (O) and heterogeneous (E) nucleation, respectively.  $I_h$  indicates hexagonal ice,  $I_c$  predominantly cubic ice, whereas  $I_h + I_c$  indicates predominantly hexagonal ice.

curvature diagram,  $T$  versus  $1/d$ , where  $d$  is the pore diameter, compiles the heterogeneous and homogeneous nucleation results from dielectric spectroscopy, DSC, and X-ray scattering. Hexagonal ice formed by heterogeneous nucleation predominates under moderate confinement. Under higher confinement characterized by a radius of curvature below 35 nm cubic ice formed by homogeneous nucleation dominates. Implicit is a correlation between the nucleation mechanism, the size of confinement and the type of ice crystals. In addition, Figure 5 includes the melting temperatures obtained from dielectric spectroscopy. The melting temperature decreases with increased confinement that, in principle, can be described by the Gibbs–Thomson (GT) equation as  $T_m(d) = T_m^{\text{bulk}} - K_{GT}/(d - d_0)$ , where  $T_m^{\text{bulk}}$  is the bulk melting temperature,  $d_0$  is the thickness of a premelted layer, and  $K_{GT}$  is a constant ( $T_m^{\text{bulk}} =$



$271.1 \pm 0.6$  K,  $K_{GT} = 76 \pm 3$  nm·K, and  $d_0 = 0.30 \pm 0.03$  nm).<sup>30</sup>

There are certain implications from this work. First, there is a correlation between homogeneous nucleation in the smaller pores and the formation of a predominant  $I_c$  form. Although earlier observations already pointed to this, the form of  $I_c$  was metastable to  $I_h$  and hence by heating there was always an irreversible transformation to the thermodynamically stable  $I_h$  phase. Under the uniform confinement provided by AAOs on the other hand,  $I_c$  is the only stable phase. We suggest that the stability of  $I_c$  reflects the relation of the critical nucleus size to the pore size. Second, the proposed phase diagram can have possible technical application in various research areas where water exists in confined spaces including construction materials like cement. For example, the occurrence of two well-defined peaks in DSC (at  $-41$  °C and  $-23$  °C) due to ice formation in hardened Portland cement pastes (water/cement ratio below 0.40) can be well-understood based on the homogeneous/heterogeneous freezing of water in different pore structures.<sup>33</sup> Third, the suppression of heterogeneous nucleation in AAO pores having diameters  $\leq 35$  nm opens up the possibility of employing AAO templates as filters for ultrapure water.

## ■ ASSOCIATED CONTENT

### ● Supporting Information

Experimental details on sample preparation and characterization and on methods. This material is available free of charge via the Internet at <http://pubs.acs.org>.

## ■ AUTHOR INFORMATION

### Corresponding Author

\*E-mail: [gfloudas@uoi.gr](mailto:gfloudas@uoi.gr).

### Notes

The authors declare no competing financial interest.

## ■ ACKNOWLEDGMENTS

The current work was supported by the operational program of the NSRF "Aristeia" cofinanced by the European Union and the Greek state. H.D. and M.S. gratefully acknowledge financial support from the German Research Foundation (SPP 1369, BU 1556/31-1, STE 1127/13, and INST 190/134-1). H.D. gratefully acknowledges Max-Planck-Gesellschaft (MPG) for the financial support of the MPIP-TOBB ETU Partner Group Program. Sample preparation by C. Hess and H. Tobergte as well as SEM investigations by M. Müller are gratefully acknowledged.

## ■ REFERENCES

- (1) Mishima, O.; Stanley, H. E. The relationship between liquid, supercooled and glassy water. *Nature* **1998**, *396*, 329–335.
- (2) Debenedetti, P. G. Supercooled and glassy water. *J. Phys.: Condens. Matter* **2003**, *15*, R1669–R1726.
- (3) Atkinson, J. D.; Murray, B. J.; Woodhouse, M. T.; Whale, T. F.; Baustian, K. J.; Carslaw, K. S.; Dobbie, S.; O'Sullivan, D.; Malkin, T. L. The importance of feldspar for ice nucleation by mineral dust in mixed-phase clouds. *Nature* **2013**, *498*, 355–358.
- (4) Creamean, J. M.; et al. Dust and biological aerosols from the Sahara and Asia influence precipitation in western U.S. *Science* **2013**, *339*, 1572–1578.
- (5) Masuda, H.; Fukuda, K. Ordered Metal Nanohole Arrays Made by a Two-Step Replication of Honeycomb Structures of Anodic Alumina. *Science* **1995**, *268*, 1466–1468.
- (6) Malkin, T. L.; Murray, B. J.; Brukhno, A. V.; Anwar, J.; Salzmann, C. G. Structure of ice crystallized from supercooled water. *Proc. Natl. Acad. Sci. U.S.A.* **2012**, *109*, 1041–1045.
- (7) Whalley, E. Scheiner's halo: Evidence of ice Ic in the atmosphere. *Science* **1981**, *211*, 389–390.
- (8) Mayer, E.; Hallbrucker, A. Cubic ice from liquid water. *Nature* **1987**, *325*, 601–602.
- (9) Huang, J.; Bartell, L. S. Kinetics of Homogeneous Nucleation in the Freezing of Large Water Clusters. *J. Phys. Chem.* **1995**, *99*, 3924–3931.
- (10) Murray, B. J.; Knopf, D. A.; Bertram, A. K. The formation of cubic ice under conditions relevant to Earth's atmosphere. *Nature* **2005**, *434*, 202–205.
- (11) Shilling, J. E.; Tolbert, M. A.; Toon, O. B.; Jensen, E. J.; Murray, B. J.; Bertram, A. K. Measurements of vapor pressure of cubic ice and their implication for atmospheric ice clouds. *Geophys. Res. Lett.* **2006**, *33*, L17801:1–5.
- (12) Arnold, G. P.; Finch, E. D.; Rabideau, S. W.; Wenzel, R. G. Neutron-diffraction study of ice polymorphism III. Ice Ic. *J. Chem. Phys.* **1968**, *49*, 4365–4369.
- (13) Hansen, T. C.; Koza, M. M.; Kuhs, W. F. Formation and annealing of cubic ice: I. Modeling of stacking faults. *J. Phys.: Condens. Matter* **2008**, *20*, 285104:1–12.
- (14) Steytler, D. C.; Dore, J. C.; Wright, C. J. Neutron Diffraction Study of Cubic Ice Nucleation in a Porous Silica Network. *J. Phys. Chem.* **1983**, *87*, 2458–2459.
- (15) Morishige, K.; Kawano, K. Freezing and melting of water in a single cylindrical pore: The pore-size dependence of freezing and melting behavior. *J. Chem. Phys.* **1999**, *110*, 4867–4872.
- (16) Dore, J. Structural studies of water in confined geometry by neutron diffraction. *Chem. Phys.* **2000**, *258*, 327–347.
- (17) Findenegg, G. H.; Jähnert, S.; Akcakayiran, D.; Schreiber, A. Freezing and melting of water confined in silica nanopores. *ChemPhysChem* **2008**, *9*, 2651–2659.
- (18) Johari, G. P. Origin of the enthalpy features of water in 1.8 nm pores of MCM-41 and the large  $C_p$  increase at 210 K. *J. Chem. Phys.* **2009**, *130*, 124518:1–6.
- (19) Tombari, E.; Johari, G. P. On the state of water in 2.4 nm cylindrical pores of MCM from dynamic and normal specific heat measurements. *J. Chem. Phys.* **2013**, *139*, 064507:1–9.
- (20) Malkin, T. L.; Murray, B. J.; Salzmann, C. G.; Molinero, V.; Pickering, S. J.; Whale, T. F. Stacking disorder in ice I. *Phys. Chem. Chem. Phys.* **2015**, *17*, 60–76.
- (21) Russo, J.; Romano, F.; Tanaka, H. New metastable form of ice and its role in the homogeneous crystallization of water. *Nat. Mater.* **2014**, *13*, 733–739.
- (22) Grigoriadis, C.; Duran, H.; Steinhart, M.; Kappl, M.; Butt, H.-J.; Floudas, G. Suppression of Phase Transitions in a Confined Rodlike Liquid Crystal. *ACS Nano* **2011**, *5*, 9208–9215.
- (23) Duran, H.; Steinhart, M.; Butt, H.-J.; Floudas, G. Arrays of Aligned Supramolecular Wires by Macroscopic Orientation of Columnar Discotic Mesophases. *ACS Nano* **2012**, *6*, 9359–9365.
- (24) Duran, H.; Steinhart, M.; Butt, H.-J.; Floudas, G. From Heterogeneous to Homogeneous Nucleation of Isotactic Poly(propylene) Confined to Nanoporous Alumina. *Nano Lett.* **2011**, *11*, 1671–1675.
- (25) Suzuki, Y.; Duran, H.; Steinhart, M.; Butt, H.-J.; Floudas, G. Homogeneous crystallization and local dynamics of poly(ethylene oxide) (PEO) confined to nanoporous alumina. *Soft Matter* **2013**, *9*, 2621–2628.
- (26) Suzuki, Y.; Duran, H.; Akram, W.; Steinhart, M.; Floudas, G.; Butt, H.-J. Multiple nucleation events and local dynamics of poly( $\epsilon$ -caprolactone) (PCL) confined to nanoporous alumina. *Soft Matter* **2013**, *9*, 9189–9198.
- (27) Suzuki, Y.; Duran, H.; Steinhart, M.; Butt, H.-J.; Floudas, G. Suppression of Poly(ethylene oxide) Crystallization in Diblock Copolymers of Poly(ethylene oxide)-b-poly( $\epsilon$ -caprolactone) Confined to Nanoporous Alumina. *Macromolecules* **2014**, *47*, 1793–1800.

- (28) Beinert, M.; Rengarajan, G. T.; Pankaj, S.; Enke, D.; Steinhart, M. Manipulating the Crystal State of Pharmaceuticals by Nanoconfinement. *Nano Lett.* **2007**, *7*, 1381–1385.
- (29) Johari, G. P. Water's size-dependent freezing to cubic ice. *J. Chem. Phys.* **2005**, *122* (194504), 1–5.
- (30) Lupi, L.; Hudait, A.; Molinero, V. Heterogeneous Nucleation of Ice on Carbon Surfaces. *J. Am. Chem. Soc.* **2014**, *136*, 3156–3164.
- (31) Johnston, J. C.; Molinero, V. Crystallization, Melting, and Structure of Water Nanoparticles at Atmospherically Relevant Temperatures. *J. Am. Chem. Soc.* **2012**, *134*, 6650–6659.
- (32) Sugisaki, M.; Suga, H.; Seki, S. *Bull. Chem. Soc. Jpn.* **1968**, *41*, 2591–2599.
- (33) Bager, D. H.; Sellevold, E. J. Ice formation in hardened cement paste, Part I- Room temperature cured pastes with variable moisture contents. *Cem. Concr. Res.* **1986**, *16*, 709–720.